


 Cite this: *RSC Adv.*, 2023, **13**, 13006

# Crystal growth and negative thermal expansion properties of a $\text{Y}_2\text{Mo}_4\text{O}_{15}$ single crystal†

 Wanling Rong, Fuan Liu,\* Xiangmei Wang, Youxuan Sun, Zeliang Gao\* and Xutang Tao 

A bulk-size single crystal of  $\text{Y}_2\text{Mo}_4\text{O}_{15}$  with  $20 \times 11 \times 8 \text{ mm}^3$  was successfully grown by the top-seed solution growth (TSSG) method. The full-width at half maximum of (100) and (010) crystal faces is 37 and 27 arcsec, respectively. The thermal conductivity coefficients  $\kappa_{11}$ ,  $\kappa_{22}$ ,  $\kappa_{33}$ , and  $\kappa_{13}$  are determined to be 1.519, 2.097, 0.445, and  $0.997 \text{ W m}^{-1} \text{ K}^{-1}$ , respectively. It is worth noting that the  $\text{Y}_2\text{Mo}_4\text{O}_{15}$  crystal shows significant anisotropy thermal expansion properties, which exhibits a negative thermal expansion along the *b*-axis ( $\alpha_{22} = -5.11 \times 10^{-6} \text{ K}^{-1}$ ). The crystal structure analysis shows that the shrinking of Mo–O bond lengths along the *b*-axis with the increasing temperature would be the main origin of the negative thermal expansion properties for  $\text{Y}_2\text{Mo}_4\text{O}_{15}$  crystal, which does not comply with the current mechanism.

 Received 27th February 2023  
Accepted 17th April 2023

DOI: 10.1039/d3ra01320k

[rsc.li/rsc-advances](https://rsc.li/rsc-advances)

## Introduction

Thermal expansion is one of the obstacles to improving the performance of high-precision instruments. The discovery of negative thermal expansion (NTE) provides the possibility to control thermal expansion, and negative thermal expansion materials also have broad application prospects in the fields of ceramics, optics, and electronic devices. Materials with excellent NTE characteristics are important and indispensable, but such materials are relatively rare. Since the emergence of research on  $\text{ZrW}_2\text{O}_8$  exhibiting NTE characteristics in a wide temperature range (0.3–1050 K),<sup>1</sup> it has opened the door for exploring a variety of NTE materials. More NTE materials such as oxides, fluorides, nitrides, cyanides, alloys, and metal–organic frameworks have been found in various compounds.

At present, the known mechanisms of NTE materials can be roughly divided into two categories. The first category is directly caused by lattice vibrations (phonons). The bridge fluorine atoms in  $\text{ScF}_3$  crystals with double coordination generate lateral thermal vibrations.<sup>2,3</sup> Therefore, the shortening of the metal spacing connecting the two ends leads to NTE. In addition, there are also  $\text{ZrW}_2\text{O}_8$ ,  $\text{ZrV}_2\text{O}_7$ , and other materials caused by the coupled rotation of rigid polyhedra,<sup>4</sup> the M–O bond has a large bond energy, which makes the bond length and bond angle in the polyhedron exhibit the characteristics of rigidity and being hard to deform. While the bond energy between the connecting rigid polyhedra is relatively weak, the M–O–M bonds

of the rigid polyhedra that drive the connection are prone to rotational coupling, resulting in shortened distance between metal atoms M and overall shrinkage. There are also NTE caused by volume shrinkage caused by the deformation of frame structure materials such as chemical formula  $\text{A}_2\text{M}_3\text{O}_{12}$  with temperature changes.<sup>5–9</sup> The second category of expansion mechanism is determined by the lattice vibration and the physical effects, such as the ferroelectricity of  $\text{PbTiO}_3$ -based compounds,<sup>10–13</sup> the ferromagnetism of Invar alloys,<sup>14–16</sup> the interface and nanoscale effects,<sup>17,18</sup> and the phase structure transitions.<sup>19–21</sup>

$\text{ZrW}_2\text{O}_8$  and  $\text{ZrV}_2\text{O}_7$  are the most well-known NTE crystals, which exhibit isotropic NTE characteristics in a wide temperature range. With similar structures to  $\text{ZrW}_2\text{O}_8$  and  $\text{ZrV}_2\text{O}_7$ , compounds of yttrium and lanthanum molybdate with a stoichiometry as  $\text{AM}_2\text{O}_{7.5}$  have been studied as NTE materials in recent years. The chemical formula of these compounds is expressed as  $\text{Y}(\text{Dy}, \text{Ho}, \text{Tm})_2\text{Mo}_4\text{O}_{15}$ , which is twice the above-mentioned  $\text{AM}_2\text{O}_{7.5}$ . Abnormal thermal expansion behaviors along the crystallographic *b*-axis have been reported for these materials.<sup>22–24</sup> However, the current research on this material mostly stays in ceramic solid solution. It is well known that the yttrium and lanthanum ions can be easily accessible for various rare-earth ion substitutions, and these molybdates would be potential laser and Raman materials. The thermal property is one of the most characteristic of optical applications. Due to the lack of bulk single crystals, the thermal properties such as total thermal expansion coefficients, thermal diffusivity, and thermal conductivity have not been studied in detail.

In this work, the  $\text{Y}_2\text{Mo}_4\text{O}_{15}$  bulk single crystal with dimensions of  $20 \times 11 \times 8 \text{ mm}^3$  was successfully grown by the top-seeded solution growth (TSSG) method. All the thermal

State Key Laboratory of Crystal Materials, Institute of Crystal Materials, Shandong University, Jinan, 250100, China. E-mail: gaozeliang@sdu.edu.cn; 202190000075@sdu.edu.cn

† Electronic supplementary information (ESI) available. See DOI: <https://doi.org/10.1039/d3ra01320k>



properties have been studied in detail in the temperature from 25 to 400 °C. The crystal exhibits significant anisotropy of thermal expansions with NTE along the *b*-axis in the temperature range from 25 to 400 °C. The crystal structure analysis at different temperatures indicates a part of Mo<sub>1</sub>-O bond contraction along the *b*-axis is the origin of NTE, which is different from the current NTE mechanisms.

## Experimental section

### Synthesis of Y<sub>2</sub>Mo<sub>4</sub>O<sub>15</sub> polycrystals

Polycrystalline Y<sub>2</sub>Mo<sub>4</sub>O<sub>15</sub> powder was prepared by the traditional solid-phase synthesis technique. High purity Y<sub>2</sub>O<sub>3</sub> and MoO<sub>3</sub> powder were fully mixed and ground according to the molar ratio of 1 : 8. Then the raw powders were pressed into 30 mm diameter and placed in a programmable Muff furnace which was preheated at 580 °C for 24 h. The control system was then set to heat up to 700 °C at a rate of 2 °C min<sup>-1</sup> and kept for 72 h, with intermittent grinding every 24 h. The powder gradually turned to white color after sintering.

### X-ray powder diffraction

The X-ray powder diffraction (XRD) data were obtained using Bruker-AXS D8 ADVANCE X-ray diffractometer (Cu-Kα = 1.54056 Å) at room temperature. The measurements were carried out in the scanning angle range of 2θ from 10° to 90° with a scanning parameter of 0.02°/0.5 s.

### Optimized crystal growth

In 2020, the Y<sub>2</sub>Mo<sub>4</sub>O<sub>15</sub> bulk single crystal was grown for the first time in our group.<sup>25</sup> However, low transparency and obvious internal cracks of crystals seriously hindered our complete characterization of the properties of the crystal. To obtain high-quality and large-dimension crystals, the flux system, viscosity, and cooling rate were optimized in this work. To decrease the flux viscosity, the ratio of the mixture of LiCO<sub>3</sub>, MoO<sub>3</sub>, and Y<sub>2</sub>O<sub>3</sub> with the molar ratio was changed from 1 : 8 : 2 to 1.5 : 10 : 2. Then the mixture was heated in a platinum crucible which was placed in a temperature controlled furnace. The temperature control program was set to heat to 960 °C at a rate of 5 °C h<sup>-1</sup>, and a platinum rod was used to stir the melt continuously for a day to achieve homogenization. The platinum wire was introduced and extended 2 mm below the surface of the melt at 805 °C, and the temperature was slowly lowered to induce spontaneous nucleation. After several times of grain-induced growth, the crystal seed along the [010] direction can be obtained. Subsequently, the crystallization temperature of 789 °C was accurately determined with an error of less than 0.5 °C. A crystal seed was gradually brought into the solution at 2 °C above the saturation temperature and maintained for an hour to melt the surface slightly. After the temperature rapidly reduced to the saturation temperature, the crystal growth was started at a cooling rate of 0.1–0.15 °C day<sup>-1</sup>. After 52 days, the single crystal was slowly lifted off and suspended above the liquid level. The programmable furnace was cooled to room temperature at a rate of no more than 8 °C h<sup>-1</sup> to avoid crystal cracking.

### Crystal quality characterization

To evaluate the crystallinity of the Y<sub>2</sub>Mo<sub>4</sub>O<sub>15</sub> crystal, high-resolution X-ray diffraction (HRXRD) was performed on the Bruker-AXSD5005HR diffractometer equipped with two-crystal Ge (220) monochromator set for Cu-Kα radiation (λ = 1.54056 Å). The (100) and (010) crystal wafers with the dimension of 4 × 4 × 1 mm<sup>3</sup> were used to measure Laue's back reflection patterns on a real-time Back reflection Laue camera system (Multiwire MWL 120 with Northstar software).

### Thermal properties

It is well known that the thermal properties of crystals are essential for crystal growth and application.<sup>26</sup> The specific heat data of Y<sub>2</sub>Mo<sub>4</sub>O<sub>15</sub> crystal was obtained by differential scanning calorimetry using a simultaneous thermal analyzer (TGA/DSC1/1600HT, MettlerToledo Inc.), with the temperature range from 25 to 300 °C at a heating rate of 10 °C min<sup>-1</sup>. The Y<sub>2</sub>Mo<sub>4</sub>O<sub>15</sub> belongs to a monoclinic system, and there are four independent thermal diffusivity, thermal expansion, and thermal conductivity coefficients. The samples used in the thermal diffusivity and thermal expansion determination were shown in Fig. 1, and they were finely polished and sprayed with 100 nm thick gold on both sides for thermal diffusivity measurement. The thermal diffusivity was determined by the laser flash method using a laser flash device (NETZSCH LFA 457 Nanoflash). The thermal dilatometer (Diamond TMA) was used to measure the thermal expansion coefficients.

## Results and discussion

### Synthesis and crystal growth of Y<sub>2</sub>Mo<sub>4</sub>O<sub>15</sub>

The purity of Y<sub>2</sub>Mo<sub>4</sub>O<sub>15</sub> polycrystalline powder was tested by X-ray diffraction analysis. As shown in Fig. 2, the XRD pattern of polycrystalline Y<sub>2</sub>Mo<sub>4</sub>O<sub>15</sub> powder obtained in the experiment accords well with the theoretical calculation results.

The single crystals obtained by spontaneous crystallization and non-oriented seed crystal growth are shown in Fig. 3a and

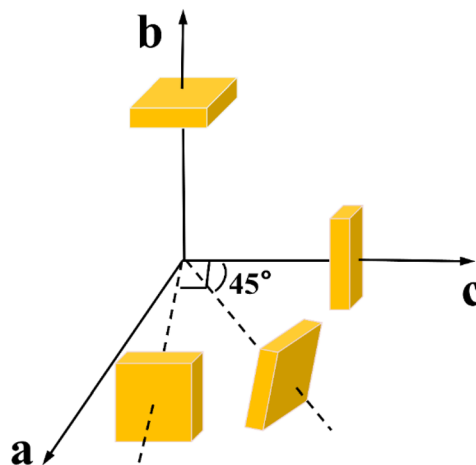


Fig. 1 Schematic diagram of four wafer processing directions of Y<sub>2</sub>Mo<sub>4</sub>O<sub>15</sub> crystal.



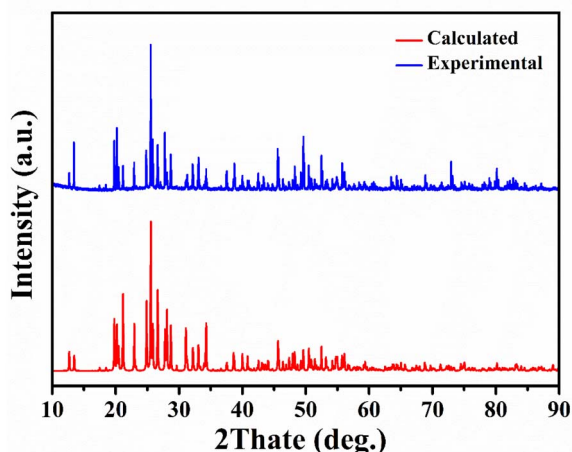


Fig. 2 Calculated and experimental powder XRD patterns of the polycrystalline  $Y_2Mo_4O_{15}$ .

b. The crystal grown with a non-oriented seed is much larger than that of spontaneous crystallization. But there are many inclusions and polycrystals in crystal, and the crystal exhibits poor transparency. It is evident from many experiments that the high viscosity of the solution resulted in many inclusions during crystal growth, but the low viscosity will also limit the crystal growth rate and growth size. Therefore, the ratio of the mixture of  $Li_2CO_3$ ,  $MoO_3$ , and  $Y_2O_3$  with It is considered that the crystal cracking is caused by the intense thermal expansion anisotropy. Therefore, it is difficult to avoid cracking or

internal quality damage of  $Y_2Mo_4O_{15}$  crystal in the process of rapid heating or cooling. In our experiments, the crystal quality can be significantly improved by reducing the cooling rate. With the optimized flux, seed crystal rotating speed, and cooling rate, the high-quality bulk  $Y_2Mo_4O_{15}$  single crystal with the size of  $20 \times 11 \times 8 \text{ mm}^3$  was successfully grown by the TSSG method along the  $[010]$  orientation as shown in Fig. 4.

### Crystal quality characterization

The rocking curves plotted for the (100) and (010) diffraction planes of the  $Y_2Mo_4O_{15}$  crystal are shown in Fig. 5a and b. They are sharp and symmetrical with full-width at half-maximum (FWHM) reaching 37 and 27 arcsec, respectively. In Fig. 5c and d, the symmetric and clear Laue diffraction patterns can be observed at four locations in each slice. Both the HRXRD and Laue diffraction results indicate the quality of the  $Y_2Mo_4O_{15}$  crystal after optimized conditions is sufficient to evaluate its intrinsic physical properties on this basis.<sup>27,28</sup>

### The specific heat

The large specific heat energy of the material is conducive to the application of crystal at high temperatures. The linear change curve of the specific heat of  $Y_2Mo_4O_{15}$  crystal as the temperature increases from 25 to 300 °C is shown in Fig. 6a (uncertainty less than 0.2%). The results indicate that the specific heat of  $Y_2Mo_4O_{15}$  crystal is  $0.43 \text{ J (g}^{-1} \text{ K}^{-1})$  at room temperature and linearly increases to  $0.73 \text{ J (g}^{-1} \text{ K}^{-1})$  at 300 °C.



Fig. 3 (a)  $Y_2Mo_4O_{15}$  grains obtained by spontaneous crystallization; (b) seedless growth of  $Y_2Mo_4O_{15}$  single crystal; (c) photo of  $Y_2Mo_4O_{15}$  single crystal after optimizing seed crystal, flux system, and viscosity.

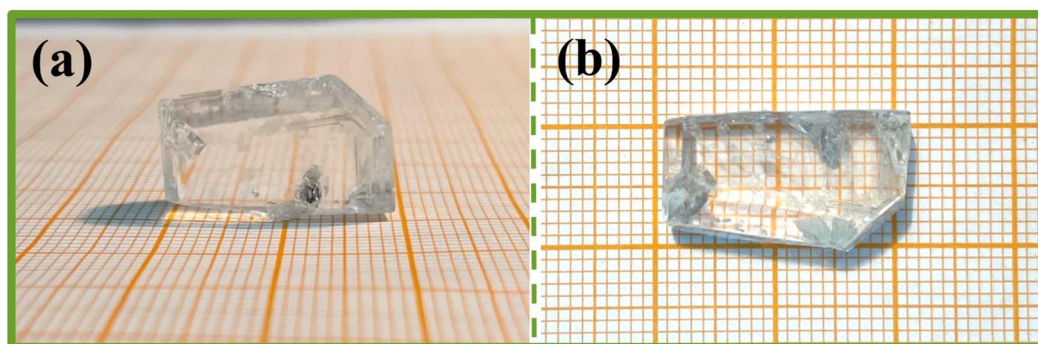


Fig. 4 (a and b) The  $Y_2Mo_4O_{15}$  single crystal under optimized crystal growth conditions.





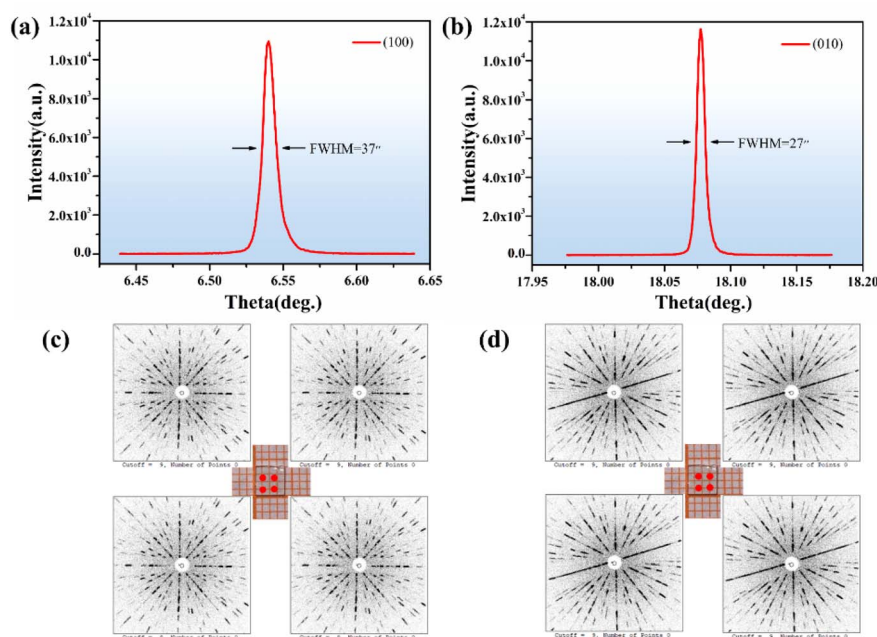


Fig. 5 (a and b) The rocking curve of the  $Y_2Mo_4O_{15}$  crystal; (c and d) Laue back-reflection patterns of (100) and (010) wafers of  $Y_2Mo_4O_{15}$  crystal.

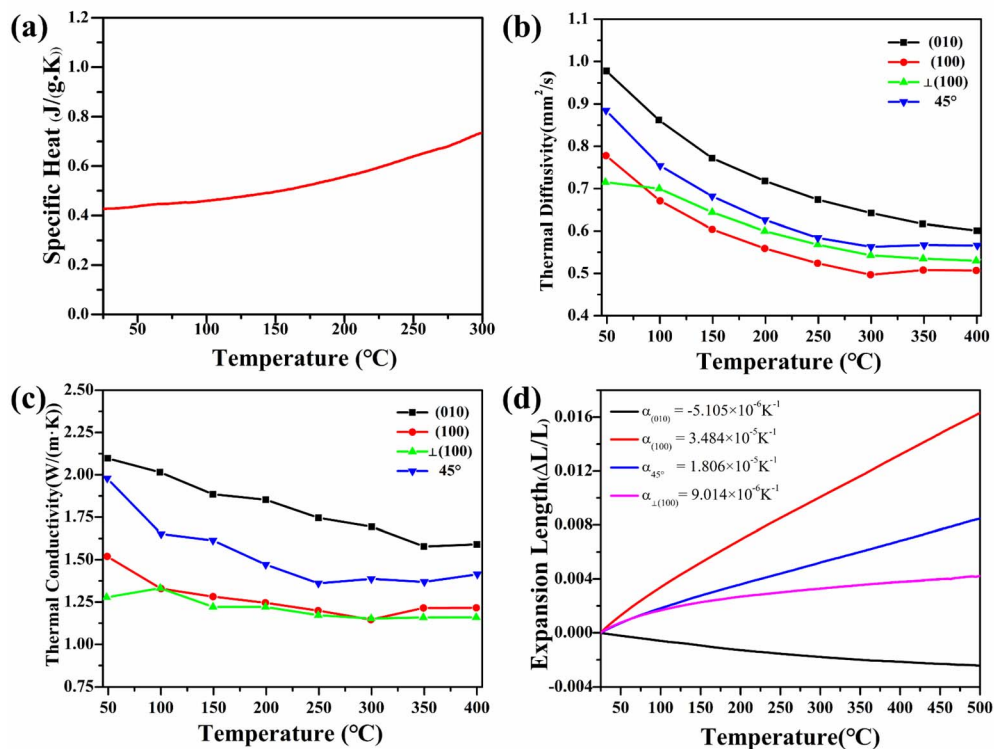


Fig. 6 (a) Temperature dependence of specific heat of  $Y_2Mo_4O_{15}$  crystal. (b) Temperature dependence of the thermal diffusivity of  $Y_2Mo_4O_{15}$  crystal. (c) Temperature dependence of the thermal conductivity of  $Y_2Mo_4O_{15}$  crystal. (d) Thermal expansion coefficients of  $Y_2Mo_4O_{15}$  crystal along different crystallographic directions.

### The thermal expansion

The thermal expansion curves along four directions from 25 to 500 °C are shown in Fig. 6d (uncertainty less than 0.1%). All the

thermal expansions of the  $Y_2Mo_4O_{15}$  crystal exhibit nearly linear changing. In the [010] direction, the expansion exhibits NTE properties. Then the average linear thermal expansion coefficients can be calculated by the following equation:



$$\bar{\alpha}(T_0 - T) = \frac{\Delta L}{L_0} \frac{1}{\Delta T} \quad (1)$$

where  $\bar{\alpha}(T_0 - T)$  is the average thermal expansion coefficient in the temperature from  $T$  to  $T_0$ ,  $L_0$  is the length of the sample at the  $T_0$ ,  $\Delta L$ , and  $\Delta T$  are the change in the length of the sample with temperature increasing from  $T$  to  $T_0$  and the range of temperature changes, respectively. At 25 °C, the thermal expansion coefficients are calculated to be  $\alpha_{(010)} = 34.8 \times 10^{-6} \text{ K}^{-1}$ ,  $\alpha_{(010)} = -5.11 \times 10^{-6} \text{ K}^{-1}$ ,  $\alpha_{\perp(100)} = 9.01 \times 10^{-6} \text{ K}^{-1}$ , and  $\alpha_{45^\circ} = 18.1 \times 10^{-6} \text{ K}^{-1}$ , respectively. According to the formula for calculating the thermal expansion ellipsoid of the monoclinic system in the literature,<sup>29</sup> the matrix of the thermal expansion coefficients can be calculated and expressed as follow:

$$\alpha_{ij} = \begin{bmatrix} \alpha_{11} & 0 & \alpha_{31} \\ 0 & \alpha_{22} & 0 \\ \alpha_{31} & 0 & \alpha_{33} \end{bmatrix} = \begin{bmatrix} 9.01 & 0 & -3.87 \\ 0 & -5.11 & 0 \\ -3.87 & 0 & 34.84 \end{bmatrix} \times 10^{-6} \quad (2)$$

The thermal expansion coefficients in the spatial distribution can be obtained with the thermal expansion coefficients. The orientation relationship between the principal axis of the thermal expansion ellipsoid and the crystallographic axis of the  $\text{Y}_2\text{Mo}_4\text{O}_{15}$  crystal is expressed in Fig. 7a. As shown in Fig. 7b, the thermal expansion coefficient of the crystal has obvious anisotropy with the transformation of the spatial orientation. Fig. 7c shows the tangent line between the  $\alpha_{11} = 0$  plane and the space-varying surface, that is, in the range of 25–500 °C, after performing the spatial rotation operation on  $\alpha_{11}$  according to the  $\theta$ - $\psi$  combination on the curve of Fig. 7c, the average thermal expansion coefficient of the spatial orientation is 0.

### The thermal diffusivity and thermal conductivity

Due to the thermal diffusivity coefficient is a second-rank symmetric tensor, four independent components need to be measured for monoclinic  $\text{Y}_2\text{Mo}_4\text{O}_{15}$  crystal. At 30–400 °C, the thermal diffusivities along four different directions are shown in Fig. 6b, and the uncertainty of measurement results is no more than 0.5%. Then the thermal conductivity can be calculated by the following equation:

$$\kappa = \lambda \rho C_p \quad (3)$$

where  $\kappa$ ,  $\lambda$ ,  $\rho$ , and  $C_p$  denote the principal thermal conductivity, thermal diffusivity, density, and the specific heat of the crystal, respectively. Like the coefficient of the thermal expansion tensor, the  $[\kappa_{ij}]$  tensor is also a symmetric second-order tensor, which is also diagonal in the main coordinate system. Therefore, we calculated the thermal conductivity of the principal axis ( $X$ ,  $Y$ ,  $Z$ ) at different temperatures. Eqn (4) below lists the spindle parameters calculated at 50 °C. The direction angle of the main axis is counterclockwise from  $Y$ -axis to the crystallographic  $c$ -axis (the  $Z$ -axis is parallel to the  $b$ -axis).

$$\kappa_{ij} = \begin{bmatrix} \kappa_{11} & 0 & \kappa_{31} \\ 0 & \kappa_{22} & 0 \\ \kappa_{31} & 0 & \kappa_{33} \end{bmatrix} = \begin{bmatrix} 1.519 & 0 & 0.997 \\ 0 & 2.097 & 0 \\ 0.997 & 0 & 0.445 \end{bmatrix} \quad (4)$$

As shown in Fig. 6c, the thermal conductivity of (100) and (001) are calculated to be 1.53  $\text{W (m}^{-1} \text{K)}$  and 2.11  $\text{W (m}^{-1} \text{K)}$  at room temperature, respectively. The thermal diffusion and thermal conductivity of  $\text{Y}_2\text{Mo}_4\text{O}_{15}$  show a decreasing trend with the increase of temperature from room temperature to 400 °C.

### Negative thermal expansion mechanism

To further explore the NTE mechanism, the crystal structures of  $\text{Y}_2\text{Mo}_4\text{O}_{15}$  crystal are analyzed at 25 °C, 50 °C, 75 °C, and 100 °C. At 25 °C, the  $\text{Y}_2\text{Mo}_4\text{O}_{15}$  crystal crystallizes in a centrally symmetric space group  $P2_1/c$  and the refined lattice parameters are  $a = 6.8185 \text{ \AA}$ ,  $b = 9.5913 \text{ \AA}$ ,  $c = 10.5299 \text{ \AA}$ ,  $\beta = 105.586^\circ$ ,  $V = 663.31 \text{ \AA}^3$  ( $Z = 2$ ), which are in good agreement with reported data.<sup>25</sup> The three-dimensional structure of the  $\text{Y}_2\text{Mo}_4\text{O}_{15}$  crystal is composed of  $\text{MoO}_4$  tetrahedron and  $\text{YO}_7$  decahedron, which are connected by O atoms like another  $\text{A}_2\text{M}_4\text{O}_{15}$  family (Fig. 8a). As shown in Fig. 8b, molybdenum atoms occupy two types of lattice position to constitute  $\text{Mo}(1)\text{O}_4$  and  $\text{Mo}(2)\text{O}_4$  tetrahedrons, respectively, while every two adjacent  $\text{Mo}(2)\text{O}_4$  tetrahedrons are connected by anti-position center  $\text{O}_{24}$  atom to form  $[\text{Mo}_2\text{O}_7]$  dimer which is similar to the  $[\text{V}_2\text{O}_7]$  group in  $\text{ZrV}_2\text{O}_7$ .

The negative thermal expansion mechanism established by detailed structural studies of  $\text{ZrV}_2\text{O}_7$  and  $\text{ZrW}_2\text{O}_8$  shows that the NTE is mainly determined by the changes in the structure of the

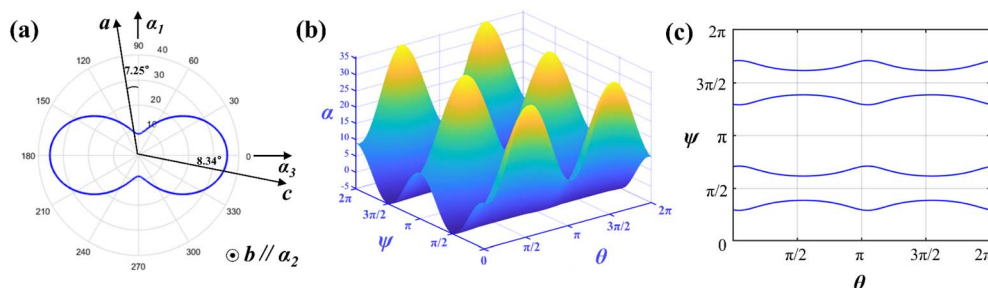


Fig. 7 (a) Thermal expansion coefficients of  $\text{Y}_2\text{Mo}_4\text{O}_{15}$  crystal in different directions on the (010) plane in polar coordinates. (b) Spatial variation of thermal expansion coefficient  $\alpha_{11}$  of  $\text{Y}_2\text{Mo}_4\text{O}_{15}$  crystal with rotation angle  $\theta$  and  $\psi$ . (c)  $\theta$ - $\psi$  matching curve with  $\alpha_{11} = 0$ .



negative ions. Considering the topological similarity between the structure of  $\text{Y}_2\text{Mo}_4\text{O}_{15}$  and the structure of  $\text{ZrV}_2\text{O}_7$  and  $\text{ZrW}_2\text{O}_8$ , it is reasonable to speculate that  $\text{Y}_2\text{Mo}_4\text{O}_{15}$  has a thermal expansion behavior mechanism similar to that of  $\text{ZrV}_2\text{O}_7$  or  $\text{ZrW}_2\text{O}_8$ .<sup>22</sup> However, according to the data in Table 1, it can be found that the bridge  $\text{Mo}_2\text{-O}_{24}\text{-Mo}_2$  bond angle always maintains  $180^\circ$ . In addition, with the increase in temperature, the bond angle between the metal atoms and the connected bridge oxygen atoms do not change significantly. Furthermore, it was observed that  $\text{O}_{14}$  in  $\text{Mo}(1)\text{O}_4$  tetrahedron is weakly connected to the  $\text{Mo}_2$  of the  $[\text{Mo}_2\text{O}_7]$  group like the connection of  $\text{O}_3$  of the  $\text{W}(2)\text{O}_4$  tetrahedron to  $\text{W}(1)$  of  $\text{WO}_4$  tetrahedron in the  $\text{ZrW}_2\text{O}_8$  structure.<sup>4</sup>

But in fact, due to the distance between  $\text{Mo}_2\cdots\text{O}_{14}$  (2.5082–2.5272 Å) in  $\text{Y}_2\text{Mo}_4\text{O}_{15}$  is much longer than that of theoretical bonding distance (1.73–2.18 Å)<sup>30</sup> and the  $\text{W}(1)\cdots\text{O}_3$  bond in  $\text{ZrW}_2\text{O}_8$  (about 2.39 Å), the  $\text{W}(1)\cdots\text{O}_3$  bond in  $\text{ZrW}_2\text{O}_8$  is thus stronger than the  $\text{Mo}_2\cdots\text{O}_{14}$  in  $\text{Y}_2\text{Mo}_4\text{O}_{15}$ . Therefore, the  $\text{O}_{14}$  atom cannot perform lateral thermal vibration as the bridge oxygen atom, which is different from the NTE mechanism of  $\text{ZrW}_2\text{O}_8$  for the thermal vibration of bridge oxygen atoms.

Table 1 Bridge bond angles ( $^\circ$ ) of  $\text{Y}_2\text{Mo}_4\text{O}_{15}$  from 25 to 100 °C

Bond	Bond angles			
	25 °C	50 °C	75 °C	100 °C
$\text{Mo}_2\text{-O}_{24}\text{-Mo}_2$	180.000(0)	180.000(0)	180.000(3)	180.000(0)
$\text{Mo}_1\text{-O}_{14}\text{-Mo}_2$	130.000(0)	129.225(4)	129.379(2)	129.447(2)
$\text{Y-O}_1\text{-Mo}_2$	143.557(4)	143.527(3)	143.474(3)	143.619(3)
$\text{Y-O}_2\text{-Mo}_1$	147.785(4)	147.870(4)	147.326(3)	148.111(3)
$\text{Y-O}_3\text{-Mo}_1$	164.748(4)	164.695(4)	164.753(4)	164.521(4)
$\text{Y-O}_4\text{-Mo}_2$	163.482(4)	163.454(4)	163.566(4)	163.830(4)
$\text{Y-O}_5\text{-Mo}_1$	144.926(4)	145.634(3)	144.852(3)	144.366(3)
$\text{Y-O}_6\text{-Mo}_1$	135.813(3)	136.206(3)	136.372(3)	136.171(3)
$\text{Y-O}_7\text{-Mo}_2$	119.675(4)	119.719(3)	119.307(3)	119.425(3)

The mechanism of NTE is further explored from the change of bond length.<sup>31,32</sup> As shown in Table 2, the bond lengths of  $\text{Y}_2\text{Mo}_4\text{O}_{15}$  from 25 °C to 100 °C are presented. The bond length of the Y–O bonds increases gradually with the temperature increasing, while the bond length of  $\text{Mo}_2\text{-O}$  remains almost unchanged. It is worth noting that the length of the  $\text{Mo}_1\text{-O}_{12}$  bond and  $\text{Mo}_1\text{-O}_{13}$  bond in the direction close to the  $b$ -axis

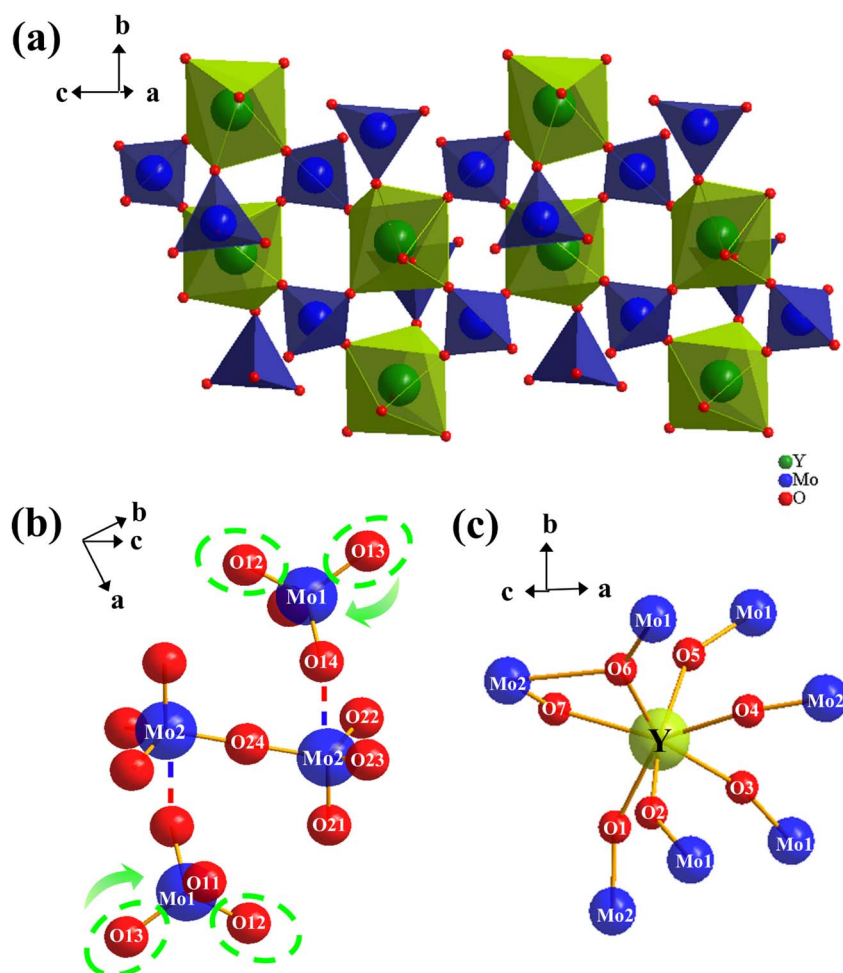


Fig. 8 (a) Schematic diagram of the common vertex connection between  $\text{MoO}_4$  tetrahedron and  $\text{YO}_7$  decahedron. (b)  $\text{Mo}_1\text{-O}$  and  $\text{Mo}_2\text{-O}$  structure in  $\text{Y}_2\text{Mo}_4\text{O}_{15}$  crystal. (c) The skeletal structure of  $\text{Y-O}$  decahedron.



Table 2 Bond lengths (Å) of  $Y_2Mo_4O_{15}$  from 25 to 100 °C ( $Mo_2-O$  and  $Y-O$  are average lengths)

Bond	Bond lengths			
	25 °C	50 °C	75 °C	100 °C
$Mo_1-O_{11}$	1.763(6)	1.752(6)	1.756(6)	1.753(6)
$Mo_1-O_{12}$	1.746(7)	1.744(7)	1.738(7)	1.744(7)
$Mo_1-O_{13}$	1.750(7)	1.748(7)	1.745(7)	1.742(7)
$Mo_1-O_{14}$	1.783(6)	1.787(6)	1.784(6)	1.788(6)
$Mo_2-O_{21}$	1.737(7)	1.732(7)	1.739(6)	1.743(6)
$Mo_2-O_{22}$	1.735(8)	1.741(8)	1.738(7)	1.744(7)
$Mo_2-O_{23}$	1.735(7)	1.739(6)	1.739(6)	1.733(6)
$Mo_2-O_{24}$	1.866(9)	1.867(9)	1.866(6)	1.867(6)
$Mo_2-O$	1.769(5)	1.769(5)	1.770(4)	1.771(6)
$Y-O$	2.298(6)	2.298(5)	2.303(6)	2.304(5)

direction shows shrinking trend, especially the length of  $Mo_1-O_{13}$  bond shrinks from 1.750(7) Å to 1.742(7) Å. The increase of  $Y-O$  bond length with increasing temperature provides the main driving force for the positive thermal expansion behaviors, while the contraction of part of the  $Mo_1-O$  bond is the main reason for the negative thermal expansion along the  $b$ -axis. The overall thermal expansion of  $Y_2Mo_4O_{15}$  is dominated by the thermal expansion of the  $a$ -axis and  $c$ -axis, showing a positive thermal expansion.

The crystal structures analysis shows that the contraction of  $Mo-O$  bonds along the  $b$ -axis with increasing temperature is the main origin of the NTE property of  $Y_2Mo_4O_{15}$  crystal, which is not similar to the current NTE mechanism.

## Conclusion

In summary, the bulk single crystal  $Y_2Mo_4O_{15}$  with  $20 \times 11 \times 8$  mm<sup>3</sup> was successfully grown by the TSSG method. The full-width at half-maximum (FWHM) of (100) and (010) faces is 37 and 27 arcsec, respectively. All the thermal properties including the specific heat, thermal diffusion, thermal expansion, and thermal conductivity are studied in detail. The results show that the  $Y_2Mo_4O_{15}$  crystal has significant anisotropy thermal properties with NTE property along the  $b$ -axis. The change of the crystal structure of  $Y_2Mo_4O_{15}$  with temperature indicates that the contraction of the  $Mo-O$  bonds along the  $b$ -axis as the temperature increases is the major contribution to the NTE property of  $Y_2Mo_4O_{15}$  crystal, which is not similar to the current NTE mechanism.

## Conflicts of interest

The authors declare no competing financial interest.

## Acknowledgements

This work is financially supported by the National Natural Science Foundation of China (62175129); Qilu Young Scholar of Shandong University; Program of Introducing Talents of Disciplines to Universities in China (111 program) (BP2018013).

## Notes and references

- 1 T. A. Mary, J. S. O. Evans, T. Vogt and A. W. Sleight, *Science*, 1996, **272**, 90–92.
- 2 C. W. Li, X. Tang, J. A. Munoz, J. B. Keith, S. J. Tracy, D. L. Abernathy and B. Fultz, *Phys. Rev. Lett.*, 2011, **107**, 195504.
- 3 B. K. Greve, K. L. Martin, P. L. Lee, P. J. Chupas, K. W. Chapman and A. P. Wilkinson, *J. Am. Chem. Soc.*, 2010, **132**, 15496–15498.
- 4 A. K. A. Pryde, K. D. Hammonds, M. T. Dove, V. Heine, J. D. Gale and M. C. Warren, *J. Phys.: Condens. Matter*, 1996, **8**, 10973–10982.
- 5 S. Sumithra, U. V. Waghmare and A. M. Umarji, *Phys. Rev. B: Condens. Matter Mater. Phys.*, 2007, **76**, 024307.
- 6 L. H. N. Rimmer and M. T. Dove, *J. Phys.: Condens. Matter*, 2015, **27**, 185401.
- 7 B. A. Marinkovic, M. Ari, P. M. Jardim, R. R. de Avillez, F. Rizzo and F. F. Ferreira, *Thermochim. Acta*, 2010, **499**, 48–53.
- 8 S. Sumithra, A. K. Tyagi and A. M. Umarji, *Mater Sci Eng B Solid State Mater Adv Technol.*, 2005, **116**, 14–18.
- 9 T. A. Mary and A. W. Sleight, *J. Mater. Res.*, 1999, **14**, 912–915.
- 10 J. Chen, F. Wang, Q. Huang, L. Hu, X. Song, J. Deng, R. Yu and X. Xing, *Sci. Rep.*, 2013, **3**, 2458.
- 11 J. Chen, X. Xing, C. Sun, P. Hu, R. Yu, X. Wang and L. Li, *J. Am. Chem. Soc.*, 2008, **130**, 1144–1145.
- 12 J. Chen, K. Nittala, J. S. Forrester, J. L. Jones, J. Deng, R. Yu and X. Xing, *J. Am. Chem. Soc.*, 2011, **133**, 11114–11117.
- 13 X. R. Xing, J. X. Deng, Z. Q. Zhu and G. R. Liu, *J. Alloys Compd.*, 2003, **353**, 1–4.
- 14 Y. Kakehashi, *J. Phys. Soc. Jpn.*, 1980, **49**, 2421–2422.
- 15 Y. Tino and Y. Iguchi, *J. Magn. Magn. Mater.*, 1983, **31–4**, 117–118.
- 16 A. Katsuki and K. Terao, *J. Phys. Soc. Jpn.*, 1969, **26**, 1109–1114.
- 17 Ismail, P. Hofmann, A. P. Baddorf and E. W. Plummer, *Phys. Rev. B: Condens. Matter Mater. Phys.*, 2002, **66**, 245414.
- 18 B. W. Busch and T. Gustafsson, *Phys. Rev. B: Condens. Matter Mater. Phys.*, 2000, **61**, 16097–16104.
- 19 J. Arvanitidis, K. Papagelis, S. Margadonna, K. Prassides and A. N. Fitch, *Nature*, 2003, **425**, 599–602.
- 20 W. C. M. Mattens, H. Holscher, G. J. M. Tuin, A. C. Moleman and F. R. Deboer, *J. Magn. Magn. Mater.*, 1980, **15–8**, 982–984.
- 21 Y. W. Long, N. Hayashi, T. Saito, M. Azuma, S. Muranaka and Y. Shimakawa, *Nature*, 2009, **458**, 60–U63.
- 22 L. Sebastian, S. Sumithra, J. Manjanna, A. M. Umarji and J. Gopalakrishnan, *Mater Sci Eng B Solid State Mater Adv Technol.*, 2003, **103**, 289–296.
- 23 H. Wang, J. Peng, X. J. Li, Y. M. Hao, D. F. Chen and Z. Hu, *Phys. B*, 2007, **388**, 278–284.
- 24 Z. Yu, D. Chen, H. Wang, J. Peng, Y. Cheng, M. Wu and Z. Hu, *Rare Met.*, 2007, **26**, 426–434.
- 25 X. Wang, Z. Gao, C. Wang, X. Guo, Y. Sun, Y. Jia and X. Tao, *RSC Adv.*, 2021, **11**, 1164–1171.



- 26 W. B. Hou, D. Xu, D. R. Yuan, M. G. Liu, N. Zhang, X. T. Tao, S. Y. Sun and M. H. Jiang, *Cryst. Res. Technol.*, 1994, **29**, 939–944.
- 27 A. Tayal, Y. Chen, C. Song, S. Hiroi, L. S. R. Kumara, N. Palina, O. Seo, M. Mukoyoshi, H. Kobayashi, H. Kitagawa and O. Sakata, *Inorg. Chem.*, 2018, **57**, 10072–10080.
- 28 H. Wu, H. Yu, W. Zhang, J. Cantwel, K. R. Poeppeliner, S. Pan and P. S. Halasyamani, *Cryst. Growth Des.*, 2017, **17**, 1404–1410.
- 29 X. J. Liu, Z. Y. Wang, X. Q. Wang, G. H. Zhang, S. X. Xu, A. D. Duan, S. J. Zhang, Z. H. Sun and D. Xu, *Cryst. Growth Des.*, 2008, **8**, 2270–2274.
- 30 J. S. O. Evans, T. A. Mary, T. Vogt, M. A. Subramanian and A. W. Sleight, *Chem. Mater.*, 1996, **8**, 2809–2823.
- 31 J. Peng, H. Wang, M. M. Wu, D. F. Chen, R. Kiyangi, J. S. Fieramosca, S. Short, J. Jorgensen and Z. Hu, *Mater. Technol.*, 2007, **22**, 33–37.
- 32 J. Peng, X. L. Xiao, Z. Hu and J. Z. Tao, *Solid State Sci.*, 2008, **10**, 1543–1548.

